

Resolution-Independent Neural Operators for Multi-Rate Sparse-View CT

Aujasvit Datta^{1,2 *}Jiayun Wang^{1 *}Asad Aali³Armeet Singh Jatyani¹Anima Anandkumar¹¹ Caltech² IIT Kanpur³ Stanford University

{peterw, armeet, anima}@caltech.edu

aujasvitd22@iitk.ac.in

asadaali@stanford.edu

Abstract

Sparse-view Computed Tomography (CT) reconstructs images from a limited number of X-ray projections to reduce radiation and scanning time, which makes reconstruction an ill-posed inverse problem. Deep learning methods achieve high-fidelity reconstructions but often overfit to a fixed acquisition setup, failing to generalize across sampling rates and image resolutions. For example, convolutional neural networks (CNNs) use the same learned kernels across resolutions, leading to artifacts when data resolution changes. We propose Computed Tomography neural Operator (CTO), a unified CT reconstruction framework that extends to continuous function space, enabling generalization (without retraining) across sampling rates and image resolutions. CTO operates jointly in the sinogram and image domains through rotation-equivariant Discrete-Continuous convolutions parametrized in the function space, making it inherently resolution- and sampling-agnostic. Empirically, CTO enables consistent multi-sampling-rate and cross-resolution performance, with on average $> 4\text{dB}$ PSNR gain over CNNs. Compared to state-of-the-art diffusion methods, CTO is $500\times$ faster in inference time with on average 3dB gain. Empirical results also validate our design choices behind CTO’s sinogram-space operator learning and rotation-equivariant convolution. Overall, CTO outperforms state-of-the-art baselines across sampling rates and resolutions, offering a scalable and generalizable solution that makes automated CT reconstruction more practical for deployment.

1. Introduction

Computed Tomography (CT) is a widely used imaging modality that reconstructs images of internal anatomy from X-ray projections acquired at multiple angles. The measured data, or sinogram, represent the line integrals of the object’s attenuation coefficient along different ray paths—mathematically modeled by the Radon transform [4, 5]. The goal of CT image reconstruction is to recover the underlying attenuation map from these projections, forming

an inverse problem: the inversion of the Radon transform. For fully sampled measurements with sufficient angular coverage, the inverse Radon transform may produce faithful reconstructions. However, in sparse-view CT, where the number of projection angles is significantly reduced and uniformly subsampled to lower radiation dose or shorter scan time [6], the inverse problem becomes ill-posed. In such cases, direct inversion leads to severe noisy artifacts, and additional regularization or learning-based methods are required to achieve high-quality reconstructions.

A classical CT reconstruction method is filtered back projection (FBP) [7], which applies a high-pass frequency filter to the sinogram, followed by a backprojection that implements the inverse Radon transform. While simple and popular, FBP produces severe artifacts with sparsely sampled measurements [8]. Iterative reconstruction methods [9–13] and later compressed sensing approaches [14–17] alleviate this by enforcing data consistency and exploiting sparsity priors, but at high computational cost. Deep learning methods such as variational networks [18, 19], and generative adversarial networks (GANs) [20] have achieved improved reconstructions. Yet, they are tied to a specific discretization setting with a fixed input measurement and output image resolution—a model trained for one measurement sampling rate or output image resolution does not generalize well to another [21, 22]. This is an impractical limitation in clinics where acquisition settings like measurement sampling rates and target resolution constantly change across organs, protocols, and diagnostic purposes. A unified model that adapts across acquisition settings would enable flexible CT reconstruction under varying conditions, thus broadening its clinical applicability.

Our approach. We consider a resolution-agnostic deep learning architecture for a unified model that works for various CT settings. We propose CTO, a unified CT reconstruction framework based on Neural Operators that learns in the infinite-dimensional function space and thus generalizes across data resolutions, including different measurement sampling rates and reconstructed image resolutions. Neural operators have demonstrated strong cross-resolution performance in tasks such as PDE solving [23, 24] and com-

*Equal contribution.

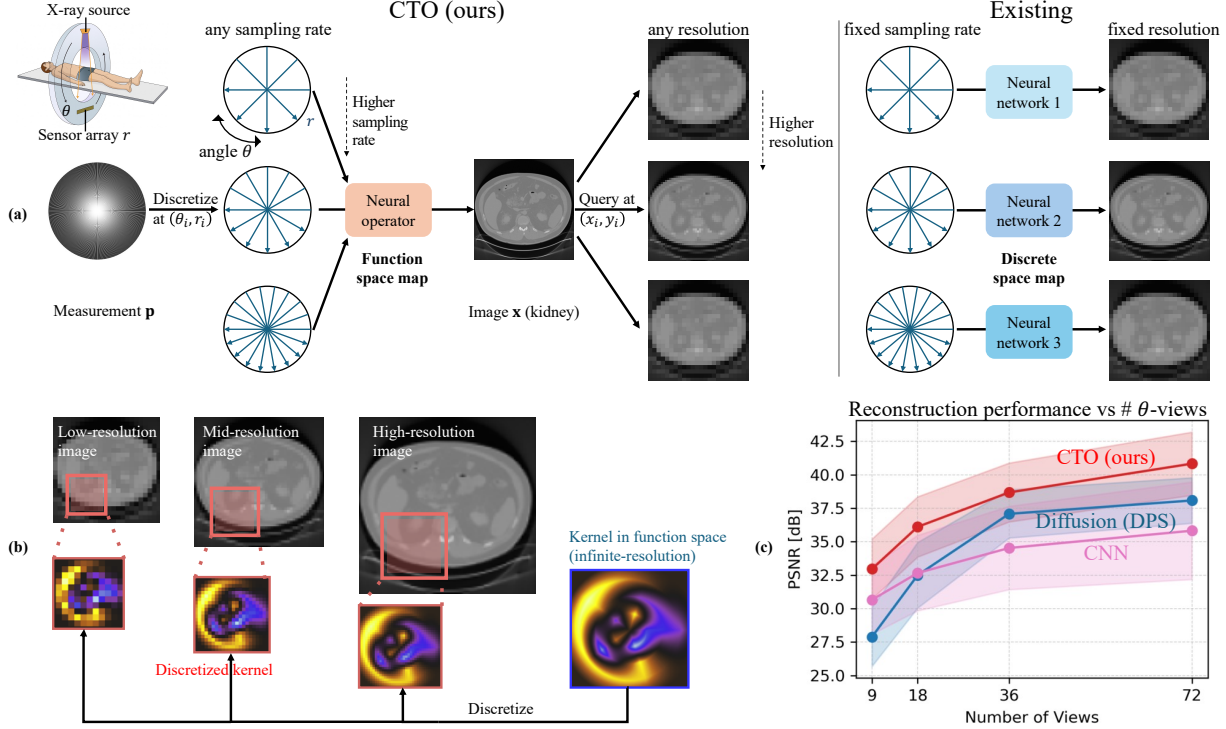


Figure 1. (a) We propose **CTO**, a unified **CT** reconstruction framework based on neural **Operator** parameterized in function space. CTO works across different measurement sampling rates, whereas existing methods based on **CNN** architecture [1] need to be trained separately for different sampling rates. (b) CTO’s basic building block is **DISCO** (discrete-continuous convolution) [2], a convolution layer defined in function space which works for images at different resolutions. Specifically, DISCO learns convolution kernels in the infinite-dimensional function space and can be discretized to a specific resolution based on the input data resolution to ensure a consistent receptive field across resolutions. (c) CTO consistently outperforms the **CNN** baseline [1] across different sampling rates for kidney CT [3]. They both follow an unrolled network design with similar model size; CTO uses resolution-independent DISCO while CNN uses regular convolutions.

putational imaging [22, 25, 26]. Among them, DISCO convolutions [23], which combine discrete and continuous representations through local integral kernels, allow scalable and resolution-independent learning—making them ideal for this setting [22, 27]. Specifically, DISCO learns infinite-dimensional function space kernels that can be discretized for different input and output data resolutions. DISCO has also been proven to be discretization-agnostic [23, 28], meaning that the error is bounded for different data resolutions and will converge to 0 when the resolution increases.

CTO uses unrolled networks with two U-shaped DISCO blocks that process the measurements and images: (NO_s) in the *sinogram domain* and (NO_i) in the *image domain*. The sinogram operator (NO_s) is defined in polar coordinates $((r, \theta))$ — the natural space of CT measurements — and jointly learns in both *spatial and frequency spaces* of sinograms, inspired by the Filtered Back Projection (FBP) algorithm [7]. The image operator (NO_i), defined on the 2D Cartesian grid, further refines spatial features and ensures high-fidelity reconstruction quality. Our framework uses DISCO [22, 23] as the basic component in both domains, enabling *resolution-agnostic* learning. Learning in the sinogram domain exploits its inherent *rotational equivariance*,

while image-domain learning enhances the spatial consistency. These components make CTO rotation-equivariant, meaning that a rotation in the measurement coordinates induces an equivalent rotation in the reconstructed image. This unified joint-domain design leads to improved generalization across sampling conditions and reconstruction resolutions. Empirically, with an architecture change from CNNs to the proposed neural operator, we observe an average of over 4 dB PSNR gain across different sinogram subsampling rates. CTO also outperforms state-of-the-art diffusion methods [29] by over 3 dB with at least 500 \times inference-time speed up. CTO also outperforms baselines in zero-shot super-resolution image reconstruction.

Our main contributions are: 1) We propose CTO, a unified end-to-end CT reconstruction framework that generalizes across measurement sampling rates and image resolutions. 2) We introduce a joint spatial-frequency learning scheme in the sinogram domain defined in polar coordinates to improve reconstruction performance and robustness. 3) CTO is inherently rotation-equivariant and resolution-agnostic through the use of DISCO operators in both sinogram and image domains, achieving consistent and high-quality reconstructions across varying conditions.

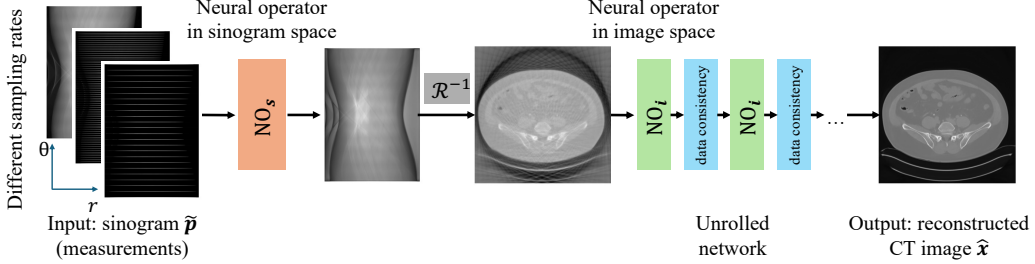


Figure 2. **CTO architecture overview.** It follows an unrolled network design (Sec.3.1). The input sensory signal sinogram was first fed to neural operator NO_s defined in sinogram space, allowing CTO to be resolution-agnostic to different sampling rates for sinograms. Then, we use unrolled networks with multiple cascades mimicking a classical iterative algorithm, with each cascade consisting of image-space NO_t and a data consistency (physical update) term. They are both defined in function space and make CTO resolution-agnostic to image resolutions. \mathcal{R}^{-1} refers to the inverse Radon transform that transforms a sinogram to an image.

2. Related works

Accelerated CT Reconstruction. Methods fall broadly into (i) *physics-based iterative* and (ii) *learning-based* approaches. Classical compressed-sensing methods impose handcrafted priors, most notably total variation (TV) and prior-image constrained CS (PICCS), to stabilize ill-posed sparse-view or limited-angle reconstructions, achieving artifact reduction but at the cost of slow multi-iteration solvers and degraded performance under extreme undersampling [17, 30, 31]. These methods highlight the *speed-fidelity trade-off* inherent to optimization-based CT. Learning-based methods instead learn data-driven priors for faster inference. Early image-domain CNNs denoise initial reconstructions (e.g., via FBP) but oversmooth details under extreme sparsity [32, 33]. Model-based unrolled networks such as Learned Primal-Dual (LPD) [19] and MoDL [34] integrate forward and adjoint operators to improve data consistency but remain tied to fixed sampling patterns, limiting adaptability. Dual-domain networks [35–41] jointly process sinogram and image domains, addressing sparse-view aliasing and fine-detail refinement, but often struggle with varying geometries or resolutions. Generative diffusion models [21, 42–45] achieve state-of-the-art performance in both sparse-view and limited-angle CT by alternating data-consistency and denoising, yet their high inference cost hinders deployment. Across these families, the central challenges remain [46]: (1) discretization binding to specific sampling rates and resolutions, (2) limited cross-geometry generalization, and (3) inference-time scalability for real-time use. Our method addresses these by introducing a neural operator formulation that learns in function space, achieving cross-resolution generalization and rotation-equivariant reconstruction without retraining.

Neural Operators for Computational Imaging. For resolution-agnostic image reconstruction, diffusion models have shown empirically stable performance across data resolutions in accelerated CT reconstruction [21, 42]. Yet, they typically incur higher inference times and require substantial hyperparameter tuning to achieve optimal results.

Further, diffusion models are not inherently discretization-agnostic. In contrast, neural operator (NO) [47, 48] is inherently resolution-agnostic as it learns a map between infinite-dimensional function spaces, enabling evaluation at arbitrary resolutions and converging toward the target operator as the grid resolution increases. NOs were first used for accelerating the numerical solutions to partial differential equations (PDEs) [24, 25, 48]. More recently, it was used for resolution-agnostic computational imaging tasks in various domains, e.g., MRI [22], neuro-imaging [27], and ultrasound imaging [25, 26]. NO architecture is tailored to each application. For instance, the Fourier NO (FNO) [49] employs global convolutions and has achieved robust discretization-agnostic performance across diverse tasks [47]. Other NOs [23, 50] use locally-supported kernels to better capture localized structures, which is beneficial in applications involving localized dynamics such as turbulent fluid modeling [50]. Additionally, NOs with local integral formulations are more amenable to parallel computation and can offer improved efficiency compared to architectures that rely on global operations. Our CT reconstruction framework leverages neural operators with local integral kernels, making it inherently agnostic to both sinogram sampling rates and output image resolution.

3. CT Reconstruction in Function Space

Overall, CTO combines unrolled networks and function space learning to allow physical awareness (of the forward operator) and resolution-agnosticism (Fig.2). Among multiple architectural designs [49, 50] available for neural operators, we choose discrete-continuous convolution (DISCO), especially for image reconstruction due to its similarity to convolutional layers. We finally present a U-shaped DISCO block, which enables a multi-scale receptive field.

3.1. CT Reconstruction with Unrolled Networks

In CT, cross-sectional images are reconstructed from a series of X-ray measurements acquired at multiple angles around an object (Fig.1a). As the beams propagate through the object, their intensity is attenuated according to the ma-

terial along each path, and detectors record this attenuation as a one-dimensional projection. Collecting projections over many angles produces a two-dimensional sinogram, which compactly represents the measurement data.

Mathematically, the sinogram can be described as a function with polar coordinates $\mathbf{p}(\theta, r)$, where θ is the projection angle and r is the detector position. The sinogram's relationship with the underlying image \mathbf{x} can be written as

$$\mathbf{p}(\theta, r) := \mathcal{R}(\mathbf{x}) + \epsilon \quad (1)$$

where \mathcal{R} is the radon transform and ϵ is the measurement noise. For a specific machine, sensor position r is fixed, but the sampling of θ varies via the programming of the scanning speed. To accelerate acquisition and reduce radiation, fewer projections are taken and measurements are subsampled as $\tilde{\mathbf{p}} = M\mathbf{p}$, where M is an angle sampling operator, which can be implemented as a binary mask that selects a subset of projection angles. Recovering the image \mathbf{x} from $\tilde{\mathbf{p}}$ becomes an ill-posed inverse problem. Classical compressed sensing methods solve the inverse problem and reconstruct the underlying image $\hat{\mathbf{x}}$ via optimization

$$\hat{\mathbf{x}} = \operatorname{argmin}_{\mathbf{x}} \frac{1}{2} \|\mathcal{A}(\mathbf{x}) - \tilde{\mathbf{p}}\|_2^2 + \lambda \Psi(\mathbf{x}) \quad (2)$$

where $\mathcal{A}(\cdot) := M\mathcal{R}$ is the linear forward operator, $\Psi(\mathbf{x})$ is a regularization term and λ is the weight of the regularization term. The optimization can be solved with gradient descent. Recently, unrolled networks [1] approximate the iterative solver by cascading learned updates; they use multiple cascades of deep learning architecture like CNNs, where a specific cascade t mimics a gradient descent step from \mathbf{x}^t to \mathbf{x}^{t+1} :

$$\mathbf{x}^{t+1} \leftarrow \mathbf{x}^t - \eta^t \mathcal{A}^*(\mathcal{A}(\mathbf{x}^t) - \tilde{\mathbf{p}}) + \lambda^t \operatorname{CNN}^t(\mathbf{x}^t) \quad (3)$$

where η^t, λ^t are weights of the data-consistency term and deep-learning-based regularization term. \mathcal{A}^* is the hermitian of the forward operator \mathcal{A} .

Reconstruction in Function Space. Both sinograms (measurements) and images are *functions*: $\mathbf{p} : \mathbb{S}^1 \times \mathbb{R} \rightarrow \mathbb{R}$ and $\mathbf{x} : \Omega \subset \mathbb{R}^2 \rightarrow \mathbb{R}$. A pixel grid is merely a discretization (sampling) of pixel value \mathbf{x} over coordinates (x, y) ; higher image resolution corresponds to denser (x, y) sampling. Likewise, acquisition with more view angles corresponds to denser sampling of θ for \mathbf{p} .

While Eqn.(2) naturally accommodates different samplings via \mathcal{A} , CNN-based unrolled networks (Eqn.(3)) optimize in a *discrete subspace* tied to a fixed grid and often overfit to that resolution. In contrast, neural operators define the learned map directly between *function spaces*, enabling a single model to act consistently across discretizations of both \mathbf{p} and \mathbf{x} . We therefore propose to replace the discrete CNN prior with an image-space neural operator NO_i :

$$\mathbf{x}^{t+1} \leftarrow \mathbf{x}^t - \eta^t \mathcal{A}^*(\mathcal{A}(\mathbf{x}^t) - \tilde{\mathbf{p}}) + \lambda^t \text{NO}_i^t(\mathbf{x}^t), \quad (4)$$

so the learned update is resolution-agnostic: the same model applies to different data discretizations (Fig.1a), i.e., different angle samplings for \mathbf{p} and to different spatial resolutions for \mathbf{x} . We choose a neural operator design specifically adopted for computational imaging as follows.

3.2. DISCO (Discrete-Continuous) Convolutions: Basic Unit for Function Space Learning

The fundamental building block of the proposed neural operator is the discrete-continuous convolution (DISCO) neural operator [23], which mimics the convolution layer but optimizes in the function space. It also provides a principled way to embed local inductive biases into neural operators while remaining resolution-agnostic. Classical CNNs achieve locality through finite-support convolutional kernels. However, a CNN layer converges to pointwise linear mappings as input resolution increases, thus losing its interpretation as local integral operators in the infinite-resolution limit [23]. This limits their ability to generalize across varying resolutions and downsampling patterns. DISCO addresses this by defining the kernel as a continuous function in the function space and discretizing it only at the resolution of the input. For a kernel κ and input g over a compact domain $D \subset \mathbb{R}^d$, the continuous convolution is given by $(\kappa * g)(v) = \int_D \kappa(u - v) g(u) du$ and is approximated by

$$(\kappa * g)(v_i) \approx \sum_{j=1}^m \kappa(u_j - v_i) g(u_j) q_j. \quad (5)$$

The kernel is parameterized as $\kappa = \sum_{\ell=1}^L \theta_\ell \kappa_\ell$ with learnable coefficients θ_ℓ and fixed basis functions κ_ℓ , where κ_ℓ is piecewise linear basis following [22] (visualized in Fig. fig:overviewb). Because the basis is defined in the function space, the convolution scales with the domain rather than the grid, converging to a local integral operator as resolution increases. This property makes DISCO an effective backbone for both NO_s and NO_i , enabling consistent feature learning across resolutions and sampling conditions.

UDNO (U-Shaped DISCO Block). UDNO [22] is a core architectural unit. Inspired by U-Net [51], it progressively downsamples to aggregate coarse contextual information and upsamples to recover fine spatial detail. U-shaped networks [51] have shown strong performance across a range of vision and medical imaging tasks [51–53] due to their ability to learn multi-scale features. UDNO builds on this design but replaces standard convolutions with DISCO layers, combining multi-scale feature learning with the resolution-agnostic properties of neural operators.

4. CTO Design Details

Framework Overview. The proposed CTO is an end-to-end model following the unrolled network architecture

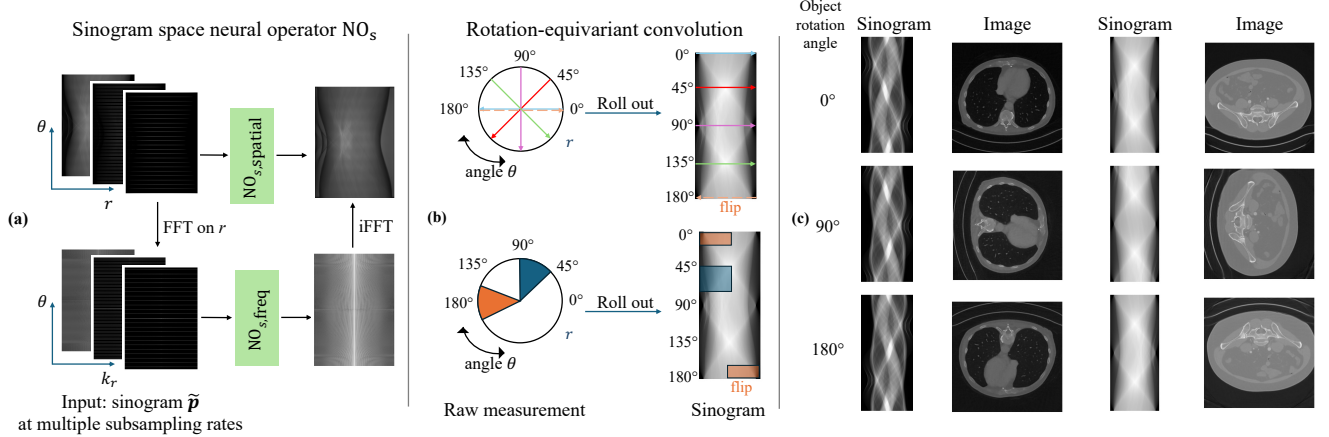


Figure 3. (a) **Sinogram-space neural operator NO_s design.** The input subsampled sinogram \tilde{p} is processed by two complementary operators: $NO_{s,\text{spatial}}$ acts in the spatial domain, while $NO_{s,\text{freq}}$ operates in the frequency domain after applying a 1D Fourier transform along the detector axis r . The outputs are combined to form the sinogram representation passed to the image-space stage. (b) **Rotation-equivariant learning in the sinogram domain.** A rotation of the object corresponds to a shift along the angular axis θ in the sinogram. By representing the sinogram in (r, θ) coordinates and enforcing circular padding along θ , the model preserves this rotational structure during learning. Note the angle flips at 180° (See π -periodicity-with-flip identity in Supplementary-Sec. A). (c) **Visualization of rotational equivariance.** We rotate the object by 0° , 90° , and 180° and obtain corresponding “rotated” sinograms (left) with CTO reconstructions (right). The reconstructions rotate consistently with the inputs, demonstrating that the rotational equivariant design of CTO enables stable and reliable reconstruction quality across different object orientations.

(Fig.2). Specifically, the input sinogram p is first fed to a sinogram space neural operator NO_s for function space learning that unifies different sampling rates for θ . The intermediate feature map is then fed to the unrolled network for multi-cascade learning, where the image-space neural operator NO_i and the physical update/data-consistency term denoise and reconstruct the final images (Eqn.(4)).

DISCO in NO_i is defined in 2D Cartesian coordinates, introducing a local inductive bias in the image space that captures fine details across discretizations. In NO_s , we extend DISCO from Cartesian to polar coordinates (r, θ) , allowing the kernels to provide localized support in the sinogram domain. Due to Radon transform duality, localized support corresponds to direction-selective global support in the image space, thus allowing NO_s to learn global structural information. Together, the two components jointly model complementary information about the image, resulting in improved structural consistency and sharper detail.

4.1. Sinogram-Space Operator NO_s

Sinogram-Space NO. We introduce a sinogram-space neural operator NO_s that acts directly on the function space of $p(\theta, r)$, with detector position r and view angle θ treated as the two sinogram axes. DISCO convolutions are applied in this native (θ, r) coordinate system—without projection or reparameterization to (x, y) —so the model learns in the inherent geometry domain of the measurements without projection errors. Extending DISCO from 2D cartesian to polar coordinates requires honoring the periodic boundary condition in θ ; we therefore use circular padding along θ (and

standard padding along r), yielding θ -shift equivariance (rotational equivariance) and consistent handling of arbitrary angular offsets. As a neural *operator*, NO_s maps between function spaces rather than fixed grids, so the same model applies across discretizations (e.g., different detector bins).

The NO_s module comprises two parallel UDNO branches (Fig.3a): $NO_{s,\text{spatial}}$ and $NO_{s,\text{freq}}$. $NO_{s,\text{spatial}}$ operates on $p(\theta, r)$ to capture local, geometry-aware correlations, while $NO_{s,\text{freq}}$ operates on the sinogram’s 2D frequency representation to model long-range angular–radial dependencies. The two outputs are averaged to form the final sinogram-space estimation, which is then forwarded to the downstream reconstruction stage. The design is inspired by a classical CT reconstruction method, FBP [7], where the additional r -frequency processing of the sinogram greatly reduces reconstruction blurriness.

Rotation-Equivariant Convolution. Parallel-beam CT induces two key symmetries on the sinogram $p(\theta, r)$: (i) rotation of the image by ϕ is a *shift in view angle* of the sinogram, $(p \circ R_\phi)(\theta, r) = p(\theta - \phi, r)$, and (ii) $p(\theta + \pi, r) = p(\theta, -r)$ (the π -periodicity-with-flip identity). We design NO_s as rotation-equivariant (details in Supplementary-A).

For implementation, NO_s adopts a circular padding along the projection angle (θ) dimension of the sinogram to account for the inherent periodicity of projection data. Projections at $\theta = 0$ and $\theta = 180^\circ$ correspond to parallel beam paths and are therefore identical up to a flip along the detector (r) axis. More generally, the projection at $\theta = 180^\circ + \alpha$ is equivalent to the projection at $\theta = \alpha$ after a flip along the detector (r) axis. To preserve this physical continuity,

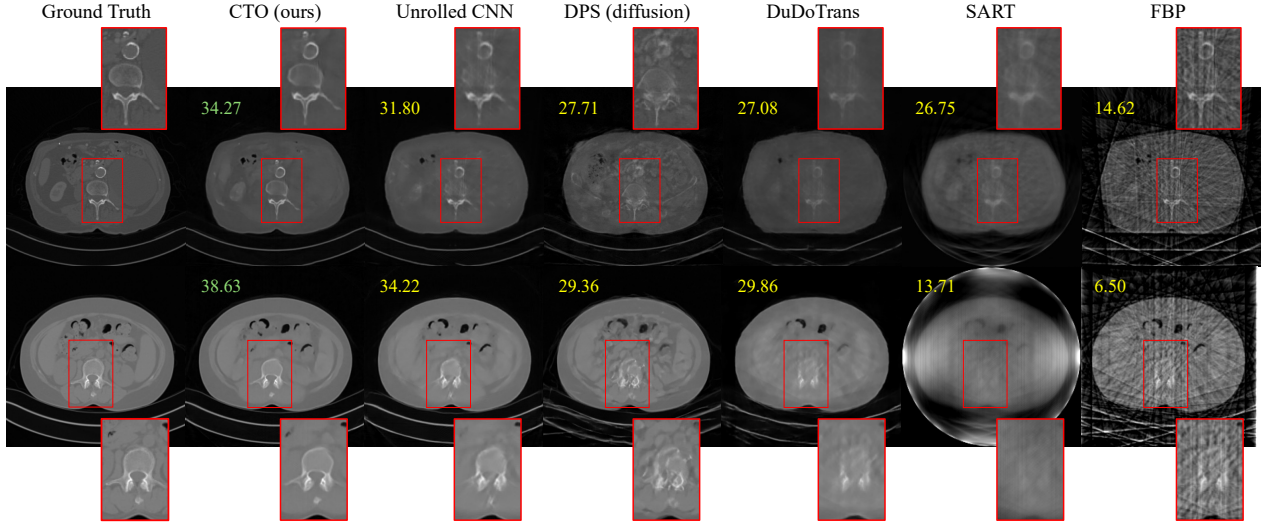


Figure 4. Reconstruction on 18-view sampling rate for Abdomen Low-Dose CT dataset [54] (top row) and Kidney dataset [3] (bottom row). CTO outperforms baselines for PSNR (upper left) and reconstruction quality.

we implement a modified circular padding scheme in which the boundary data is flipped along the detector (r) axis before being wrapped around in the projection angle (θ) axis.

We visualize the equivariant design in Fig.3b. This design choice is significant for two reasons. 1) it provides physically consistent boundary conditions in NO_s , preventing discontinuities at $\theta = 0$ and $\theta = 180^\circ$ and the artifacts they can cause. 2) It enhances rotational robustness by aligning the network’s inductive biases with the geometry of the sinogram domain. Since DISCO operators in NO_s act over the (r, θ) axes, which we treat as rectangular axes for NO learning, rotational transformations of the image x manifest as translations along these axes, which can be naturally modeled by the translational equivariance of DISCO. As this periodicity arises only along the angular dimension, we apply flipped circular padding along θ and standard reflective padding along r .

UDNO for Spatial Sinogram. $\text{NO}_{s,\text{spatial}}$ is a UDNO with circular padding, which learns in the spatial domain of the sinogram. Mathematically, its output $\hat{\mathbf{p}}_{\text{spatial}}$ can be written as $\hat{\mathbf{p}}_{\text{spatial}} = \text{NO}_{s,\text{spatial}}(\tilde{\mathbf{p}})$.

UDNO for Sinogram’s Frequency Component. To learn in the frequency domain of the sinogram, we first apply a one-dimensional Fourier transform along the detector (r) axis of the sinogram. The transformed representation is then processed by the circular-padded UDNO $\text{NO}_{s,\text{freq}}$, after which an inverse Fourier transform is applied along the same axis to return the output to the spatial domain. The overall output $\hat{\mathbf{p}}_{\text{freq}}$ can be written as $\hat{\mathbf{p}}_{\text{freq}} = \mathcal{F}_r^{-1}(\text{NO}_{s,\text{freq}}(\mathcal{F}_r(\tilde{\mathbf{p}}(r, \theta))))$.

This design is motivated by two complementary considerations. First, the Fourier slice theorem provides a theoretical foundation for learning in this domain. The theorem states that the one-dimensional Fourier transform of the projection along r satisfies

$$\mathcal{F}_r\{\mathbf{p}(\theta, r)\}(\omega) = \hat{f}(\omega \cos \theta, \omega \sin \theta), \quad (6)$$

where $\hat{f}(\xi_x, \xi_y)$ is the two-dimensional Fourier transform of the object. This result implies that the Fourier transform of the sinogram encodes the object’s frequency spectrum in polar coordinates. Consequently, localized operations in this domain correspond to global modifications in the reconstructed image, allowing $\text{NO}_{s,\text{freq}}$ to learn high-level global features about the underlying image.

Second, classical reconstruction algorithms such as FBP incorporate an explicit prior on the frequency domain of the sinogram by applying fixed frequency-domain filters (such as the ramp filter) to the one-dimensional Fourier transform of the sinogram along the detector (r) axis, suppressing low-frequency components before backprojection. Our approach can be interpreted as a data-driven generalization of this idea: rather than imposing a hand-crafted prior, $\text{NO}_{s,\text{freq}}$ learns a frequency-domain prior directly from data. This learned prior captures how it should be inpainted under different subsampling conditions, thus reducing image artifacts and enabling the model to generalize better.

Final Output. The final output of NO_s is given by, $\text{NO}_s(\tilde{\mathbf{p}}) = \frac{\hat{\mathbf{p}}_{\text{spatial}} + \hat{\mathbf{p}}_{\text{freq}}}{2}$, which is then passed downstream for processing in the image domain.

4.2. Image-Space NO_i

NO_i is implemented as a UDNO (Sec.3.2) that operates directly in the spatial domain of the image space. DISCO allows NO_i to train and infer at any image resolution. NO_i refines/denoises the intermediate reconstruction obtained from the sinogram-space operator by capturing high-frequency local information and finer structural details that may not be fully recovered in earlier stages. This ensures final reconstructions preserve multi-scale features, including large-scale structural consistency and small-scale details.

5. Experimental Results

5.1. Dataset and Setup

Datasets: We consider two CT datasets in the paper:

- **Kidney CT Scan Dataset** [3] is from 2019 Kidney and Kidney Tumor Segmentation Challenge (C4KC-KiTS). For each CT volume, we select the central 50% of slices and a uniform 10% sample of peripheral slices to ensure coverage across anatomical variability. This results in 33,000 training slices from 170 patients. For evaluation, we use 10,000 slices from 40 held-out patients.
- **AAPM Low-Dose Abdominal CT Dataset** [54] consists of 5,936 axial slices with patient ID. Following the split in [40, 41], we select 90% of patients for training and the rest (526 slices) for testing.

5.2. Reconstruction with Different Sampling Rates

CTO Implementation. CTO follows unrolled networks [1] with 3 cascades. Each cascade consists of an image-space operator (NO_i) followed by a data consistency module. All UDNOs (Sec. 3.2) share the same architectural configuration: DISCO parameterized with a piecewise-linear kernel basis [22] composed of one isotropic basis and 5 anisotropic basis rings, each containing 7 basis functions (hyperparameter-tuned, CNN baseline matches the model size). Each UDNO uses one input and one output channel, 32 hidden channels, and four encoder-decoder (pooling) levels. The DISCO kernels use a radius cutoff of 0.02 and are defined over an input domain of size 256×256 . Models are trained using mean squared error (MSE) loss with the Adam optimizer and a learning rate of 0.001.

Baseline: Unrolled CNN uses the same number of cascades and channels as CTO, with DISCOs replaced by regular convolutions. Unrolled CNN can be considered an ablation study that compares neural operator (function space) and neural network (discrete space) architecture.

Baseline: Transformer. DuDoTrans [40] uses transformer architecture that jointly enhances sinograms and images.

We provide details of other baseline implementations and sinogram sampling settings in Supplementary Sec. B.

Hardware and Training. The training of our model and baselines is with a batch size of 16 across 4 A100 (40GB) GPUs. We follow the baseline papers’ other settings.

Evaluation Protocols. CT images represent linear attenuation coefficients that are typically interpreted in *Hounsfield Units* (HU), where water is defined as 0 HU and air as -1000 HU. Following [43], we report RMSE after converting reconstructed images to HU to provide a clinically meaningful measure of reconstruction error. We also report PSNR and SSIM in the original reconstruction space (before HU conversion) to assess structural and perceptual fidelity independent of scanner calibration. Thus, RMSE (HU) reflects quantitative clinical accuracy, while PSNR

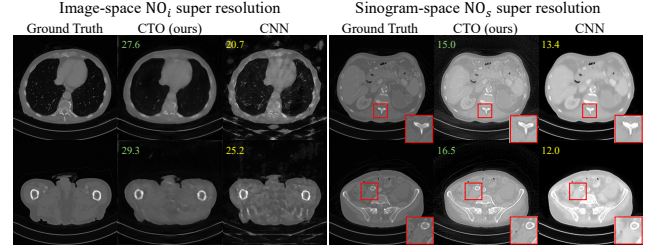


Figure 5. Zero-shot super resolution results. CTO outperforms CNN baseline for both NO_i and NO_s super resolution.

and SSIM capture image similarity.

Multi-Sparse-View Rate Results. We evaluate reconstruction performance at 9, 18, 36, and 72-view acquisition settings, where fewer projections correspond to lower radiation at the cost of more ill-posed reconstruction. A single model is trained jointly over all sampling rates, with each rate being encountered equally during training. Results for the C4KC-KiTS dataset [3] are shown in Table 1 and Fig.1c.¹ Results for the AAPM abdomen dataset [54] are shown in Supplementary-Table 3. Visual comparisons with 18-view subsampling are in Fig.4. Visualizations of multiple sampling rates are in Supplementary-Fig.6.

CTO outperforms learning-free methods [7, 10] and deep learning methods, including both diffusion methods [29, 55] and architectures like CNNs [1] and transformers [40]. On the kidney dataset [3], on average across different no. of views, we perform 1) 4 dB PSNR better than unrolled CNN baseline; 2) 3 dB PSNR better than diffusion-DPS [29]; 3) 5 dB better than transformer-DuDoTrans [40]. On the abdomen dataset [54], we perform 1) 3 dB PSNR better than unrolled CNN baseline; 2) 6 dB better than DPS [29]; 3) 6 dB better than DuDoTrans [40] on average.

5.3. Zero-Shot Super-Resolution Results

Super-Resolution on NO_i . We evaluate NO ’s zero-shot super-resolution in the image domain by training both CTO and the Unrolled CNN baseline [1] on 256×256 reconstructions obtained from 18-view sinograms. At inference, we keep the sinogram-space operator NO_s unchanged and bilinearly upsample the intermediate 256×256 reconstruction to 512×512 before applying NO_i (or the image-space CNN cascades for the Unrolled CNN). We directly evaluate models without fine-tuning against fully sampled 512×512 bilinearly interpolated ground truth images. For the CNN baseline, the absolute kernel size remains the same, and the ratio of kernel size over feature map size is halved, while the ratio of NO stays the same. Compared to the CNN baseline, CTO achieves a 3 dB PSNR gain for NO_i -superresolution. Visualizations in Fig.5 demonstrate that

¹Due to the long inference time of diffusion models, we report evaluation metrics on a random subset of 500 slices from 10,000 slices to ensure apples-to-apples comparison across methods. Full test-set results for non-diffusion baselines are included in Supplementary Sec. C.

Table 1. Sparse-view CT reconstruction results for kidney CT dataset [3]. Lower is better for RMSE; higher is better for PSNR/SSIM.

Category	Method	18-view			36-view			72-view		
		RMSE (HU)↓	PSNR↑	SSIM (x10 ⁻²)↑	RMSE (HU)↓	PSNR↑	SSIM (x10 ⁻²)↑	RMSE (HU)↓	PSNR↑	SSIM (x10 ⁻²)↑
Learning-free	FBP [7]	1541.70 ± 190.59	6.74 ± 1.45	5.00 ± 3.00	1502.42 ± 185.69	6.96 ± 1.45	8.78 ± 2.81	1423.67 ± 175.85	7.43 ± 1.45	16.54 ± 2.48
	SART [10]	678.26 ± 140.11	14.13 ± 3.09	48.93 ± 6.60	678.86 ± 144.47	14.16 ± 3.27	50.93 ± 7.61	675.58 ± 145.43	14.22 ± 3.35	51.00 ± 8.84
Diffusion	DPS [29]	81.67 ± 21.72	32.50 ± 2.45	88.03 ± 4.10	47.25 ± 8.73	37.08 ± 1.80	94.38 ± 1.63	41.95 ± 6.99	38.08 ± 1.70	95.34 ± 1.53
	ALD [55]	92.26 ± 16.09	31.25 ± 1.72	85.58 ± 3.15	53.21 ± 8.97	36.02 ± 1.63	93.27 ± 1.80	43.28 ± 6.70	37.79 ± 1.59	95.27 ± 1.53
Single pass	DudoTrans [40]	111.86 ± 25.87	29.62 ± 2.07	84.64 ± 5.19	64.69 ± 16.01	34.42 ± 2.18	90.94 ± 3.85	48.03 ± 13.06	37.04 ± 2.37	94.49 ± 3.19
	GloReDi [41]	108.36 ± 84.92	30.76 ± 3.86	85.28 ± 7.42	94.30 ± 86.62	32.19 ± 4.09	87.76 ± 7.11	84.60 ± 88.21	33.37 ± 4.32	90.01 ± 7.15
	Unrolled CNN [1]	82.52 ± 41.09	32.66 ± 2.82	89.54 ± 3.33	67.67 ± 38.30	34.53 ± 3.11	91.92 ± 3.12	60.65 ± 43.93	35.82 ± 3.64	93.84 ± 2.95
	CTO (ours)	53.50 ± 13.55	36.11 ± 2.25	92.56 ± 2.50	39.67 ± 9.59	38.68 ± 2.20	94.85 ± 1.85	31.07 ± 8.11	40.83 ± 2.36	96.42 ± 1.55

Table 2. Inference and tuning time of methods tested on NVIDIA A100. NO is at least 500× faster than diffusion [55].

Category	Method	Inference Time (s)	Tuning Required
Learning-free	SART [10]	0.417	✓
Diffusion	DPS [29]	51.58	✓
	ALD [55]	32.72	✓
Single-pass	CTO (ours)	0.065	✗

while the CNN baseline exhibits substantial blurring and aliasing artifacts at 512×512 resolution, CTO preserves reconstruction quality and gives a noticeably higher PSNR. **Super-Resolution on NO_s.** To test the zero-shot super-resolution performance of NO_s, we consider the increased view angle θ setting. Specifically, CTO is only trained on a 72-view sinogram while inferred on a 144-view sinogram. The baseline CNN also adopts the same train/inference setting. We observe that the CTO model gives a gain of 3.5 dB PSNR over the CNN baseline in NO_s super-resolution experiments. Visualizations in Fig.5 show that CTO preserves fine anatomical structures with fewer artifacts and substantially higher PSNR as compared to CNNs.

5.4. Analysis and Ablation Study

Model Inference and Tuning Time. We compare the model development and inference time of our end-to-end neural operator (NO) with diffusion models (2): Diffusion models require pattern-specific hyperparameter tuning and are at least 500× slower in inference. Classical learning-free methods like SART [10] still require hyperparameter tuning for specific p sampling rates during optimization.

Rotational Equivariance. We perform an ablation study to evaluate the impact of rotational equivariance design (via circular padding). As in Sec. 4.1, circular padding enforces the periodic boundary conditions inherent to the sinogram’s angular domain and enables the network to better exploit rotational equivariance. Supplementary Table 5 shows that rotation equivariance design leads to 0.83 PSNR under a 24-view subsampling setting. Qualitative results (Fig.3c) demonstrate that the reconstruction rotates as the object rotates. Our equivariance design gives a notable improvement in PSNR, indicating that handling angular periodicity explicitly enhances the overall reconstruction quality.

Design Choices for Frequency-Domain Learning in the Sinogram Space. To determine the most effective configuration for frequency-space learning, we evaluate different Fourier transform strategies for the sinogram prior to operator learning by NO_{s,freq}. Specifically, we consider four variants: 1) **Detector-axis transform:** one-dimensional Fourier transform applied along the detector (r) axis. 2) **Angle-axis transform:** one-dimensional Fourier transform applied along the angular (θ) axis. 3) **2D transform:** two-dimensional Fourier transform applied along both detector and angular axes. 4) **Baseline (no transform):** no frequency-space learning is applied, and the network operates only in the spatial domain of the sinogram and image.

The comparative results of these configurations are summarized in Supplementary-Fig.7. We observe that incorporating frequency-space learning in any form leads to a consistent boost in reconstruction quality compared to purely spatial-domain learning (1dB gain). Among the variants, applying the Fourier transform along the detector axis provides the largest performance gain, consistent with the theoretical advantages of this strategy as detailed in Sec. 4.1.

6. Summary

We present CTO, a unified neural operator-based framework for sparse-view CT reconstruction that generalizes across different sampling rates of sensory data, overcoming the limitations of existing deep learning methods, which are tied to fixed acquisition settings. Specifically, we adopt the Neural Operator, a deep learning framework that learn maps between infinite-dimensional function spaces and thus is agnostic to different data resolutions. By combining rotation-equivariant discrete-continuous convolutions (DISCO) (a specific neural operator design that closely mimics convolutions but uses function-space kernels) with joint spatial-frequency learning in the sinogram domain, CTO achieves robust, resolution-agnostic reconstructions and consistently outperforms state-of-the-art methods across varying downsampling regimes, enabling a scalable and flexible alternative to traditional CT reconstruction techniques. Future work could extend CTO to 3D CT and other computational imaging tasks, as well as evaluate its performance on additional datasets to further validate its generalization and clinical applicability.

Acknowledgment

This work is supported in part by ONR (MURI grant N000142312654 and N000142012786). A.D. is supported in part by the Undergraduate Research Fellowships (SURF) at Caltech. J.W. is supported in part by the Pritzker AI+Science initiative and Schmidt Sciences. A.A. is supported in part by Bren endowed chair and the AI2050 senior fellow program at Schmidt Sciences.

References

- [1] Hemant K. Aggarwal, Merry P. Mani, and Mathews Jacob. Modl: Model-based deep learning architecture for inverse problems. *IEEE Transactions on Medical Imaging*, 38(2):394–405, February 2019. [2](#), [4](#), [7](#), [8](#), [13](#), [14](#)
- [2] Jeremy Ocampo, Matthew A Price, and Jason D McEwen. Scalable and equivariant spherical cnns by discrete-continuous (disco) convolutions. *arXiv preprint arXiv:2209.13603*, 2022. [2](#), [12](#)
- [3] Nicholas Heller, Niranjan Sathianathan, Arveen Kalapara, Edward Walczak, Keenan Moore, Heather Kaluzniak, Joel Rosenberg, Paul Blake, Zachary Rengel, Makinna Oestreich, et al. The kits19 challenge data: 300 kidney tumor cases with clinical context, ct semantic segmentations, and surgical outcomes. *arXiv preprint arXiv:1904.00445*, 2019. [2](#), [6](#), [7](#), [8](#), [14](#)
- [4] Shady Hermena and Michael Young. Ct-scan image production procedures. *StatPearls*, 2023. [1](#)
- [5] Johann Radon. 1.1 über die bestimmung von funktionen durch ihre integralwerte längs gewisser mannigfaltigkeiten. *Classic papers in modern diagnostic radiology*, 5(21):124, 2005. [1](#)
- [6] Yoseob Han and Jong Chul Ye. Framing u-net via deep convolutional framelets: Application to sparse-view ct. *IEEE transactions on medical imaging*, 37(6):1418–1429, 2018. [1](#)
- [7] Lawrence A Shepp and Benjamin F Logan. The fourier reconstruction of a head section. *IEEE Transactions on nuclear science*, 21(3):21–43, 1974. [1](#), [2](#), [5](#), [7](#), [8](#), [12](#), [13](#), [14](#)
- [8] Sajid Abbas, Taewon Lee, Sukyoung Shin, Rena Lee, and Seungryong Cho. Effects of sparse sampling schemes on image quality in low-dose ct. *Medical physics*, 40(11):111915, 2013. [1](#)
- [9] Richard Gordon, Robert Bender, and Gabor T Herman. Algebraic reconstruction techniques (art) for three-dimensional electron microscopy and x-ray photography. *Journal of theoretical Biology*, 29(3):471–481, 1970. [1](#)
- [10] Anders H Andersen and Avinash C Kak. Simultaneous algebraic reconstruction technique (sart): a superior implementation of the art algorithm. *Ultrasonic imaging*, 6(1):81–94, 1984. [7](#), [8](#), [12](#), [13](#), [14](#)
- [11] Hakan Erdogan and Jeffrey A Fessler. Ordered subsets algorithms for transmission tomography. *Physics in Medicine & Biology*, 44(11):2835, 1999.
- [12] Kenneth Lange, Richard Carson, et al. Em reconstruction algorithms for emission and transmission tomography. *J Comput Assist Tomogr*, 8(2):306–16, 1984.
- [13] Jean-Baptiste Thibault, Ken D Sauer, Charles A Bouman, and Jiang Hsieh. A three-dimensional statistical approach to improved image quality for multislice helical ct. *Medical physics*, 34(11):4526–4544, 2007. [1](#)
- [14] Emmanuel J Candès, Justin Romberg, and Terence Tao. Robust uncertainty principles: Exact signal reconstruction from highly incomplete frequency information. *IEEE Transactions on information theory*, 52(2):489–509, 2006. [1](#)
- [15] David L Donoho. Compressed sensing. *IEEE Transactions on information theory*, 52(4):1289–1306, 2006.
- [16] Emil Y Sidky and Xiaochuan Pan. Image reconstruction in circular cone-beam computed tomography by constrained, total-variation minimization. *Physics in Medicine & Biology*, 53(17):4777, 2008.
- [17] Guang-Hong Chen, Jie Tang, and Shuai Leng. Prior image constrained compressed sensing (piccs): a method to accurately reconstruct dynamic ct images from highly undersampled projection data sets. *Medical physics*, 35(2):660–663, 2008. [1](#), [3](#)
- [18] Kyong Hwan Jin, Michael T McCann, Emmanuel Froustey, and Michael Unser. Deep convolutional neural network for inverse problems in imaging. *IEEE transactions on image processing*, 26(9):4509–4522, 2017. [1](#)
- [19] Jonas Adler and Ozan Öktem. Learned primal-dual reconstruction. *IEEE transactions on medical imaging*, 37(6):1322–1332, 2018. [1](#), [3](#)
- [20] Franz Thaler, Kerstin Hammernik, Christian Payer, Martin Urschler, and Darko Štern. Sparse-view ct reconstruction using wasserstein gans. In *International workshop on machine learning for medical image reconstruction*, pages 75–82. Springer, 2018. [1](#)
- [21] Jiaming Liu, Rushil Anirudh, Jayaraman J Thiagarajan, Stewart He, K Aditya Mohan, Ulugbek S Kamilov, and Hyojin Kim. Dolce: A model-based probabilistic diffusion framework for limited-angle ct reconstruction. In *Proceedings of the IEEE/CVF international conference on computer vision*, pages 10498–10508, 2023. [1](#), [3](#)
- [22] Armeet Singh Jatyani, Jiayun Wang, Aditi Chandrashekhar, Zihui Wu, Miguel Liu-Schiavini, Bahareh Toloochams, and Anima Anandkumar. A unified model for compressed sensing mri across undersampling patterns. In *Proceedings of the Computer Vision and Pattern Recognition Conference*, pages 26004–26013, 2025. [1](#), [2](#), [3](#), [4](#), [7](#)
- [23] Miguel Liu-Schiavini, Julius Berner, Boris Bonev, Thorsten Kurth, Kamyar Azizzadenesheli, and Anima Anandkumar. Neural operators with localized integral and differential kernels. *arXiv preprint arXiv:2402.16845*, 2024. [1](#), [2](#), [3](#), [4](#)
- [24] Chuwei Wang, Julius Berner, Zongyi Li, Di Zhou, Jiayun Wang, Jane Bae, and Anima Anandkumar. Coarse graining with neural operators for simulating chaotic systems, 2025. [1](#), [3](#)
- [25] Jiayun Wang, Yousuf Aborahama, Arya Khokhar, Yang Zhang, Chuwei Wang, Karteekeya Sastry, Julius Berner, Yilin Luo, Boris Bonev, Zongyi Li, Kamyar Azizzadenesheli, Lihong V. Wang, and Anima Anandkumar. Accelerating 3d photoacoustic computed tomography with end-to-end physics-aware neural operators, 2025. [2](#), [3](#)

[26] Jiayun Wang, Oleksii Ostras, Masashi Sode, Bahareh Tolooshams, Zongyi Li, Kamyar Azizzadenesheli, Giandomenico F Pinton, and Anima Anandkumar. Ultrasound lung aeration map via physics-aware neural operators. *ArXiv*, pages arXiv–2501, 2025. 2, 3

[27] Bahareh Tolooshams, Lydia Lin, Thierri Callier, Jiayun Wang, Sanvi Pal, Aditi Chandrashekhar, Claire Rabut, Zongyi Li, Chase Blagden, Sumner L Norman, et al. Vars-fusi: Variable sampling for fast and efficient functional ultrasound imaging using neural operators. *bioRxiv*, pages 2025–04, 2025. 2, 3

[28] Julius Berner, Miguel Liu-Schiaffini, Jean Kossaifi, Valentin Duruisseaux, Boris Bonev, Kamyar Azizzadenesheli, and Anima Anandkumar. Principled approaches for extending neural architectures to function spaces for operator learning. *arXiv preprint arXiv:2506.10973*, 2025. 2

[29] Hyungjin Chung, Jeongsol Kim, Michael Thompson McCann, Marc Louis Klasky, and Jong Chul Ye. Diffusion posterior sampling for general noisy inverse problems. In *The Eleventh International Conference on Learning Representations*, 2023. 2, 7, 8, 13, 14

[30] Yan Liu, Zhengrong Liang, Jianhua Ma, Hongbing Lu, Ke Wang, Hao Zhang, and William Moore. Total variation-stokes strategy for sparse-view x-ray ct image reconstruction. *IEEE transactions on medical imaging*, 33(3):749–763, 2013. 3

[31] Zhengshan Yu, Xingya Wen, and Yan Yang. Reconstruction of sparse-view x-ray computed tomography based on adaptive total variation minimization. *Micromachines*, 14(12):2245, 2023. 3

[32] Dong Hye Ye, Gregory T Buzzard, Max Ruby, and Charles A Bouman. Deep back projection for sparse-view ct reconstruction. In *2018 ieee global conference on signal and information processing (globalsip)*, pages 1–5. IEEE, 2018. 3

[33] Chengzhu Zhang, Yincheng Li, and Guang-Hong Chen. Accurate and robust sparse-view angle ct image reconstruction using deep learning and prior image constrained compressed sensing (dl-piccs). *Medical physics*, 48(10):5765–5781, 2021. 3

[34] Hemant K Aggarwal, Merry P Mani, and Mathews Jacob. Modl: Model-based deep learning architecture for inverse problems. *IEEE transactions on medical imaging*, 38(2):394–405, 2018. 3

[35] Wei-An Lin, Haofu Liao, Cheng Peng, Xiaohang Sun, Jing-dan Zhang, Jiebo Luo, Rama Chellappa, and Shaohua Kevin Zhou. Dudonet: Dual domain network for ct metal artifact reduction. In *Proceedings of the IEEE/CVF Conference on Computer Vision and Pattern Recognition*, pages 10512–10521, 2019. 3

[36] Bo Zhou, Xiongchao Chen, S Kevin Zhou, James S Duncan, and Chi Liu. Dudodr-net: Dual-domain data consistent recurrent network for simultaneous sparse view and metal artifact reduction in computed tomography. *Medical Image Analysis*, 75:102289, 2022.

[37] Bo Zhou, Xiongchao Chen, Huidong Xie, S Kevin Zhou, James S Duncan, and Chi Liu. Dudoufnet: Dual-domain under-to-fully-complete progressive restoration network for simultaneous metal artifact reduction and low-dose ct reconstruction. *IEEE transactions on medical imaging*, 41(12):3587–3599, 2022.

[38] Hong Wang, Yuexiang Li, Haimiao Zhang, Jiawei Chen, Kai Ma, Deyu Meng, and Yefeng Zheng. Indudonet: An interpretable dual domain network for ct metal artifact reduction. In *International Conference on Medical Image Computing and Computer-Assisted Intervention*, pages 107–118. Springer, 2021.

[39] Chang Sun, Yazdan Salimi, Neroladaki Angeliki, Sana Boudabbous, and Habib Zaidi. An efficient dual-domain deep learning network for sparse-view ct reconstruction. *Computer methods and programs in biomedicine*, 256:108376, 2024.

[40] Ce Wang, Kun Shang, Haimiao Zhang, Qian Li, and S Kevin Zhou. Dudotrans: dual-domain transformer for sparse-view ct reconstruction. In *International workshop on machine learning for medical image reconstruction*, pages 84–94. Springer, 2022. 7, 8, 13, 14

[41] Zilong Li, Chenglong Ma, Jie Chen, Junping Zhang, and Hongming Shan. Learning to distill global representation for sparse-view ct. In *Proceedings of the IEEE/CVF international conference on computer vision*, pages 21196–21207, 2023. 3, 7, 8, 13, 14

[42] Chenchun Zhou, Yubao Sun, Jing Liang, Jia Liu, and Qingshan Liu. Sparse-view ct image reconstruction using conditional embedding fusion diffusion model. *Neurocomputing*, page 131748, 2025. 3

[43] Jixiang Chen, Yiqun Lin, Yi Qin, Hualiang Wang, and Xiaomeng Li. Cross-view generalized diffusion model for sparse-view ct reconstruction. In *International Conference on Medical Image Computing and Computer-Assisted Intervention*, pages 140–150. Springer, 2025. 7

[44] Bowen Song, Jason Hu, Zhaoxu Luo, Jeffrey Fessler, and Liyue Shen. Diffusionblend: Learning 3d image prior through position-aware diffusion score blending for 3d computed tomography reconstruction. *Advances in Neural Information Processing Systems*, 37:89584–89611, 2024.

[45] Jia Wu, Jinzhao Lin, Xiaoming Jiang, Wei Zheng, Lisha Zhong, Yu Pang, Hongying Meng, and Zhangyong Li. Dual-domain deep prior guided sparse-view ct reconstruction with multi-scale fusion attention. *Scientific Reports*, 15(1):16894, 2025. 3

[46] Shuaiqi Cheng, Yuxi Chen, Bo Yang, Chao Liu, Lijuan Zhang, Lirong Yin, and Wenfeng Zheng. Deep learning for sparse-view ct reconstruction: A survey. *Available at SSRN 5366340*, 2025. 3

[47] Kamyar Azizzadenesheli, Nikola Kovachki, Zongyi Li, Miguel Liu-Schiaffini, Jean Kossaifi, and Anima Anandkumar. Neural operators for accelerating scientific simulations and design. *Nature Reviews Physics*, pages 1–9, 2024. 3

[48] Nikola Kovachki, Zongyi Li, Burigede Liu, Kamyar Azizzadenesheli, Kaushik Bhattacharya, Andrew Stuart, and Anima Anandkumar. Neural operator: Learning maps between function spaces with applications to pdes. *Journal of Machine Learning Research*, 24(89):1–97, 2023. 3

[49] Zongyi Li, Nikola Kovachki, Kamyar Azizzadenesheli, Burigede Liu, Kaushik Bhattacharya, Andrew Stuart, and

Anima Anandkumar. Fourier neural operator for parametric partial differential equations. 2021. [3](#)

[50] Zongyi Li, Nikola Kovachki, Kamyar Azizzadenesheli, Burigede Liu, Kaushik Bhattacharya, Andrew Stuart, and Anima Anandkumar. Neural operator: Graph kernel network for partial differential equations. 2020. [3](#)

[51] Olaf Ronneberger, Philipp Fischer, and Thomas Brox. U-net: Convolutional networks for biomedical image segmentation. In *International Conference on Medical image computing and computer-assisted intervention*, pages 234–241. Springer, 2015. [4](#), [13](#)

[52] Florinel-Alin Croitoru, Vlad Hondru, Radu Tudor Ionescu, and Mubarak Shah. Diffusion models in vision: A survey. *IEEE transactions on pattern analysis and machine intelligence*, 45(9):10850–10869, 2023.

[53] William Peebles and Saining Xie. Scalable diffusion models with transformers. In *Proceedings of the IEEE/CVF international conference on computer vision*, pages 4195–4205, 2023. [4](#)

[54] Cynthia McCollough. Overview of the low dose ct grand challenge. *Medical physics*, 43(6Part35):3759–3760, 2016. [6](#), [7](#), [13](#), [14](#), [15](#)

[55] Ajil Jalal, Marius Arvinte, Giannis Daras, Eric Price, Alexandros G Dimakis, and Jon Tamir. Robust compressed sensing mri with deep generative priors. *Advances in neural information processing systems*, 34:14938–14954, 2021. [7](#), [8](#), [13](#), [14](#)

[56] Yang Song, Jascha Sohl-Dickstein, Diederik P Kingma, Abhishek Kumar, Stefano Ermon, and Ben Poole. Score-based generative modeling through stochastic differential equations. *arXiv preprint arXiv:2011.13456*, 2020. [14](#)

[57] Tero Karras, Miika Aittala, Timo Aila, and Samuli Laine. Elucidating the design space of diffusion-based generative models. *Advances in neural information processing systems*, 35:26565–26577, 2022. [14](#)

Resolution-Independent Neural Operators for Multi-Rate Sparse-View CT

Supplementary Material

In this supplementary material, we provide details omitted in the main text, including:

- Section **A**: more mathematical details of the proposed rotational equivariant DISCO. (Sec. 4.1 “Sinogram-Space Neural Operator NO_s ” of the main paper.)
- Section **B**: additional details on experimental setup, specifically sinogram sampling setting, and implementation details of baseline methods (Sec. 5.2 “Implementation Details of Different-Sampling-Rate Reconstruction” of the main paper.)
- Section **C**: more experimental results and visualizations of the method, including numerical results/tables that cannot fit in the main text due to page limit, as well as additional reconstruction visualizations of multiple methods under different sampling rates. (Sec. 5 “Experimental Results” of the main paper.)

A. Rotational Equivariant DISCO

We describe the rotational equivariant DISCO [2] design details below.

Rotation-equivariant convolution in (r, θ) . Parallel-beam CT induces two key symmetries on the sinogram $\mathbf{p}(\theta, r)$: (i) a rotation of the image by ϕ is a *shift in view angle* of the sinogram,

$$(\mathbf{p} \circ R_\phi)(\theta, r) = \mathbf{p}(\theta - \phi, r), \quad (7)$$

and (ii) the π -periodicity-with-flip identity

$$\mathbf{p}(\theta + \pi, r) = \mathbf{p}(\theta, -r). \quad (8)$$

Define the group action of in-plane rotations T_ϕ on sinogram functions by

$$(T_\phi f)(\theta, r) := f(\theta - \phi, r), \quad (9)$$

with the identification

$$f(\theta + \pi, r) \equiv f(\theta, -r). \quad (10)$$

Let \star denote a stationary convolution on (θ, r) (implemented by DISCO with quadrature),

$$(f \star \psi)(\theta, r) = \int_{\mathbb{R}} \int_0^\pi f(\theta - \tau, r - \rho) \psi(\tau, \rho) d\tau d\rho, \quad (11)$$

where the domain obeys Eqn.(8). Then \star is $SO(2)$ -equivariant with respect to the action Eqn.(9):

$$((T_\phi f) \star \psi)(\theta, r) = \int \int f(\theta - \phi - \tau, r - \rho) \psi(\tau, \rho) d\tau d\rho \quad (12)$$

$$= (f \star \psi)(\theta - \phi, r) \quad (13)$$

$$= (T_\phi(f \star \psi))(\theta, r). \quad (14)$$

In the discrete DISCO implementation, (12) holds up to the usual quadrature error.

Padding to realize the symmetry. Eqns.(7)–(12) require boundary conditions consistent with Eqn.(8). We therefore use *flipped circular padding* along θ : when indices cross the $\theta = 0/\pi$ boundary, we wrap the data while flipping r ,

$$\mathbf{p}(\theta \pm \pi, r) \mapsto \mathbf{p}(\theta, -r), \quad (15)$$

and apply standard reflective padding along r . This enforces physical continuity at $\theta = 0$ and $\theta = \pi$, prevents seam artifacts, and makes the DISCO convolutions in NO_s intrinsically rotation-robust: rotations of x become θ -translations of p (Eqn.(7)), which are naturally handled by the translational equivariance of Eqn.(11).

B. Implementation Details

B.1. Sinogram Sampling Settings

For both datasets, we generate ground-truth sinograms using 720 projection angles. For the C4KC-KiTS dataset, we use a parallel-beam geometry with a 256×256 image resolution and a detector size of 300. Projection angles are uniformly sampled over $[0, \pi]$, which is standard for parallel-beam CT. For the AAPM Low-Dose CT dataset, we use a fan-beam geometry with a 256×256 resolution and 672 detector elements, with a source-to-detector distance of 1075. Projection angles are uniformly sampled over $[0, 2\pi)$ to match the acquisition geometry of the dataset. In both datasets, we evaluate reconstruction performance at 9-view, 18-view, 36-view, and 72-view acquisition settings by subsampling the corresponding number of projection angles from the 720-view ground-truth sinograms.

B.2. Baseline Setup

1. **Learning-free iterative methods.** We include two classical reconstruction baselines: Filtered Back-Projection (FBP) [7] and the Simultaneous Algebraic Reconstruction Technique (SART) [10]. FBP reconstruction applies the inverse Radon transform configured as in Sec. B.1 on the subsampled sinograms after passing them through a ramp frequency filter. For SART, we use the public `scikit-image iradon_sart` operator. For each test image, we perform one initial SART sweep followed by four additional refinement iterations (five total). The relaxation parameter is left at the default internal setting of `iradon_sart`. Following standard conventions, all SART updates are clipped to the valid attenuation range $[0, 0.549]$ to avoid divergence.

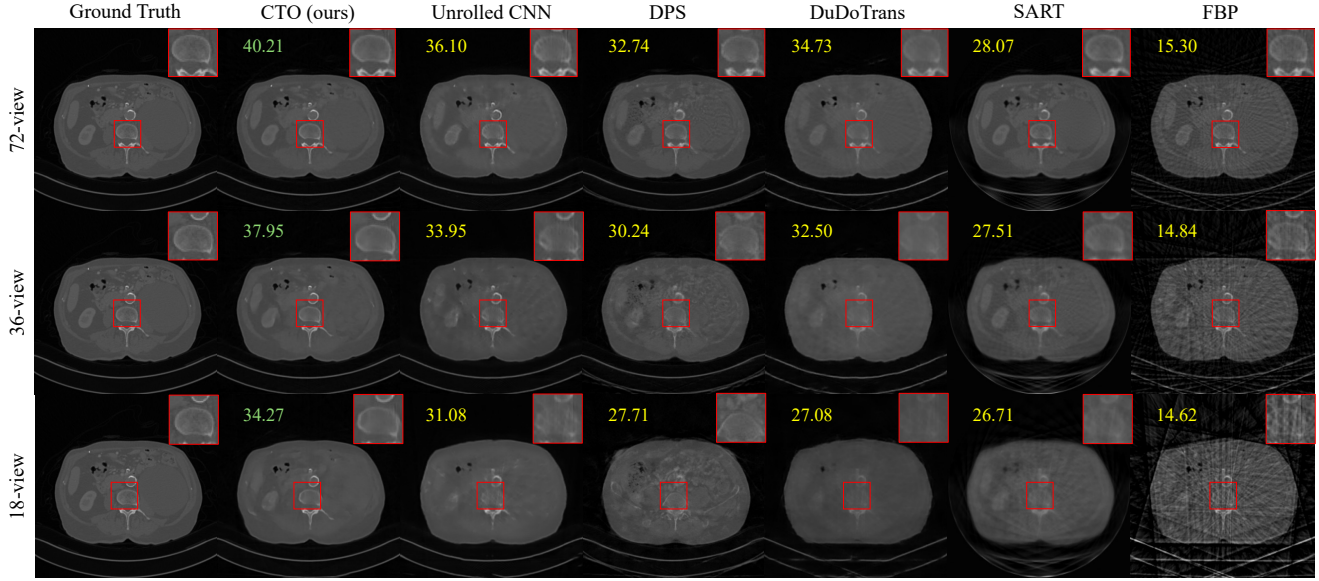


Figure 6. Reconstruction on multiple sampling rates for Abdomen Low-Dose CT dataset [54]. CTO outperforms baseline methods for PSNR (upper left) and reconstruction quality across all sinogram sampling rates.

Table 3. Sparse-view CT reconstruction results for AAPM abdominal Low Dose CT dataset [54]. Lower is better for RMSE; higher is better for PSNR/SSIM. All methods are reported on the entire test set.

Category	Method	18-view			36-view			72-view		
		RMSE (HU)↓	PSNR↑	SSIM ($\times 10^{-2}$) ↑	RMSE (HU)↓	PSNR↑	SSIM ($\times 10^{-2}$) ↑	RMSE (HU)↓	PSNR↑	SSIM ($\times 10^{-2}$) ↑
Learning-free	FBP [7]	632.58 ± 42.17	13.14 ± 1.63	33.87 ± 6.32	616.656 ± 41.07	13.36 ± 1.63	36.07 ± 5.89	584.72 ± 38.87	13.82 ± 1.63	40.35 ± 5.66
	SART [10]	161.91 ± 5.93	24.97 ± 1.46	59.51 ± 4.53	145.15 ± 2.59	25.91 ± 1.41	69.09 ± 3.37	133.24 ± 1.81	26.66 ± 1.40	76.85 ± 2.06
Diffusion	DPS [29]	149.97 ± 17.34	25.68 ± 1.77	60.08 ± 8.28	100.50 ± 7.33	29.13 ± 1.51	76.71 ± 4.02	75.19 ± 4.71	31.64 ± 1.43	82.61 ± 2.94
	ALD [55]	148.13 ± 14.63	25.78 ± 1.71	63.42 ± 7.19	110.19 ± 8.78	28.33 ± 1.46	75.50 ± 3.92	85.17 ± 5.35	30.56 ± 1.41	80.47 ± 3.12
Single pass	DudoTrans [40]	154.64 ± 6.18	25.36 ± 1.50	69.52 ± 4.32	92.17 ± 3.59	29.88 ± 1.62	78.21 ± 3.59	69.28 ± 4.99	32.35 ± 1.57	81.49 ± 3.38
	GloReDi [41]	96.89 ± 10.39	29.47 ± 1.70	78.52 ± 3.69	74.42 ± 6.24	31.74 ± 1.64	83.59 ± 3.05	64.63 ± 4.34	32.96 ± 1.55	85.78 ± 2.60
	Unrolled CNN [1]	100.65 ± 11.36	29.14 ± 1.84	78.21 ± 5.47	74.44 ± 8.32	31.76 ± 1.80	82.01 ± 4.95	62.38 ± 11.16	33.35 ± 1.81	84.49 ± 5.27
	CTO (ours)	75.97 ± 7.32	31.57 ± 1.73	81.62 ± 4.02	50.79 ± 4.27	35.06 ± 1.64	87.14 ± 3.12	36.64 ± 2.44	37.88 ± 1.56	91.55 ± 1.81

2. **Unrolled networks with CNNs.** We use an unrolled U-Net [51] baseline composed of 3 image space cascades, where each cascade consists of a U-Net refinement module followed by a data consistency update. This baseline operates entirely in the image space and does not apply any learned processing in the sinogram domain. The U-Net uses a standard encoder-decoder configuration with 32 hidden channels and four pooling levels. The model is trained under the same loss function and optimization settings as our method to ensure a fair comparison.
3. **DuDoTrans.** DuDoTrans [40] is a dual-domain sparse-view CT reconstruction framework that jointly enhances sinograms and images. A Sinogram Restoration Transformer (SRT) models long-range dependencies in the projection domain to restore informative sinograms, which are converted to an intermediate image through a differentiable consistency layer and fused with an initial FBP reconstruction. A Residual Image Reconstruc-

tion Module then refines the fused representation to produce the final output. We use the official implementation, training for 100 epochs with Adam (initial learning rate $1e-4$) and a step decay (learning rate multiplied by 0.1 after epoch 20).

4. **GloReDi.** GloReDi [41] is an image-domain framework for sparse-view CT that distills global representations (GloRe) from intermediate-view reconstructions to improve sparse-view quality. The teacher network (intermediate) guides the student (sparse) through EMA-updated weights. We use the official implementation, training for 100 epochs with Adam ($\alpha = 1e-4$).
5. **Diffusion models.** Diffusion probabilistic models (DPMs) have been shown as robust methods for solving ill-posed inverse problems. In such inverse problems, we aim to recover x_0 from corrupted measurements y , requiring sampling from the posterior $p(x_0|y)$. This stochastic process is modeled by a stochastic differential

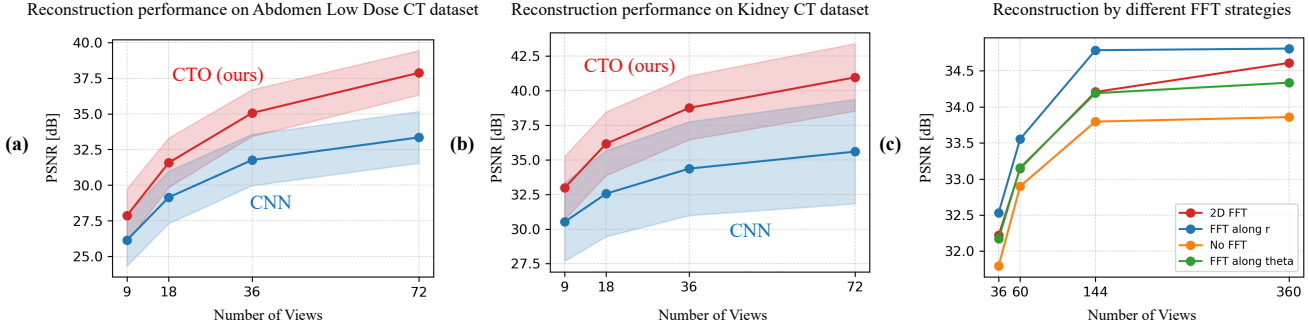


Figure 7. (a) Reconstruction performance on the AAPM abdomen Low-Dose CT dataset [54] (entire test set). (b) Reconstruction performance on the Kidney CT dataset [3] (entire test set). In both datasets, CTO consistently outperforms the CNN baseline across all sampling rates. (c) Comparison of reconstruction performance under four frequency-space configurations: 1) 2D FFT: 2D Fourier transform across both axes; 2) FFT along r : 1D Fourier transform along the detector (r) axis; 3) No FFT: no Fourier transform (spatial-domain learning only). 4) FFT along θ : 1D Fourier transform along the angular (θ) axis; Introducing frequency-space processing yields consistent improvements over the spatial-only baseline, with detector-axis transforms providing the largest gains, in line with the analysis in Sec 4.1.

Table 4. Sparse-view CT reconstruction results for Kidney CT dataset [3] for the larger test set of 10,000 images. Diffusion models are omitted due to high computational costs. Lower is better for RMSE; higher is better for PSNR/SSIM.

Category	Method	18-view			36-view			72-view		
		RMSE (HU)↓	PSNR↑	SSIM ($\times 10^{-2}$) ↑	RMSE (HU)↓	PSNR↑	SSIM ($\times 10^{-2}$) ↑	RMSE (HU)↓	PSNR↑	SSIM ($\times 10^{-2}$) ↑
Learning-free	FBP [7]	1539.09 ± 198.54	6.83 ± 1.89	5.20 ± 3.46	1499.88 ± 193.44	7.05 ± 1.89	8.97 ± 3.27	1421.26 ± 183.22	7.52 ± 1.89	16.72 ± 2.94
	SART [10]	675.36 ± 142.01	14.24 ± 3.30	49.08 ± 7.84	675.91 ± 146.27	14.27 ± 3.47	51.08 ± 7.94	672.58 ± 147.23	14.33 ± 3.54	51.19 ± 9.16
Single pass	DudoTrans [40]	112.77 ± 27.57	29.63 ± 2.14	84.61 ± 5.32	65.34 ± 17.20	34.42 ± 2.25	90.88 ± 3.99	48.52 ± 14.22	37.05 ± 2.40	94.41 ± 3.26
	GloReDi [41]	111.95 ± 92.06	30.68 ± 4.04	85.08 ± 7.81	97.92 ± 93.81	32.10 ± 4.28	87.57 ± 7.51	88.50 ± 95.46	33.24 ± 4.52	89.74 ± 7.54
	Unrolled CNN [1]	82.51 ± 48.28	32.56 ± 3.11	89.48 ± 3.50	70.74 ± 45.33	34.37 ± 3.39	91.82 ± 3.35	63.13 ± 45.85	35.60 ± 3.77	93.71 ± 3.26
	CTO (ours)	53.60 ± 13.81	36.17 ± 2.30	92.63 ± 2.55	39.71 ± 10.05	38.76 ± 2.31	94.93 ± 1.88	30.85 ± 8.08	40.97 ± 2.44	96.49 ± 1.50

equation (SDE) [56, 57]: $dx = -2\dot{\sigma}(t)(\mathbb{E}[x_0|x_t, y] - x_t)dt + g(t)dw$. Because computing likelihood $p(y|x_t)$ is computationally intractable, we use approximations, such as Diffusion Posterior Sampling (DPS) [29] and Annealed Langevin Dynamics (ALD) [55], that leverage DPMs as priors for accelerated reconstruction and approximate $p(y|x_t)$ as $p(y|x_0 = \mathbb{E}[x_0|x_t])$. For the diffusion baseline, we train a DPM following the EDM [57] loss formulation. The model was trained for 2,000 iterations, employing a UNet-style architecture comprising 65 million trainable parameters, where the learning rate, noise schedule, and training were set following [57]. For inference, we utilize a 1,000-step noise schedule (data-consistency weighting parameter $\gamma = 5e - 3$), and use the trained DPM to perform reconstruction across both approximation methods: (i) DPS [29] and (ii) ALD [55].

C. Additional Results and Visualizations

C.1. Full Test Set Results

AAPM abdominal Low Dose CT dataset. Results for the AAPM abdominal Low Dose CT dataset [54] are provided in Table 3. We also plot the numerical results in Fig.7a. All methods are reported on the entire test set.

Kidney CT dataset. We also provide results on the larger test set of 10,000 images for the Kidney CT dataset [3] in Table 4. We also plot the numerical results in Fig.7b.

We omit diffusion models from our evaluation on the larger test set due to their high computational costs. We visualize the results in Fig.7a.

C.2. Rotational Equivariance Results

We perform an ablation study to evaluate the impact of circular padding on reconstruction quality. As discussed in Section 4.1, circular padding enforces the periodic boundary conditions inherent to the sinogram’s angular domain and enables the network to better exploit rotational equivariance. Table 5 shows the reconstruction performance with and without circular padding under a 24-view subsampling setting. Incorporating circular padding leads to a notable improvement in PSNR, indicating that handling angular periodicity explicitly enhances the overall reconstruction quality.

C.3. Sinogram Space NO_s Design Variants

As discussed in Sec. 5, we evaluate several frequency-space configurations for NO_{s,freq}. Fig.7c compares four strategies: (1) 1D FFT along the detector (r) axis, (2) 1D FFT along the angular (θ) axis, (3) a 2D FFT across both axes,

Table 5. Ablation study demonstrating the effect of the proposed rotational equivariant DISCO (via circular padding) on reconstruction quality.

Method	PSNR on 24-view subsampled reconstruction (dB)
CTO	33.00
CTO (no Rot. Eqv.)	32.17

and (4) a spatial-domain baseline without any transform. All frequency-space variants improve reconstruction quality over the baseline, with the detector-axis transform yielding the largest gain, consistent with the analysis in Sec. 4.1.

C.4. Multi-Rate Visualization

Fig.6 shows reconstructions on the AAPM abdomen low-dose CT dataset [54] across multiple sampling rates. CTO preserves reconstruction quality even under heavy undersampling with noticeably fewer artifacts compared to other methods.